

## Fibre corrosion in uncracked high-performance fibre reinforced cementitious composites

Mylene M. Vieira<sup>a,b,\*</sup>, Sergio H.P. Cavalaro<sup>c</sup>, Antonio Aguado<sup>d</sup>, Dimas A.S. Rambo<sup>e</sup>, Renan P. Salvador<sup>e</sup>

<sup>a</sup> Department of Civil Engineering, Campus Russas, Federal University of Ceará, UFC, Felipe Santiago 411, 62900-000 Russas, Brazil

<sup>b</sup> CAPES Foundation, Ministry of Education of Brazil, Brasília, DF 70040-020, Brazil

<sup>c</sup> School of Architecture, Building and Civil Engineering, Loughborough University, Leicestershire LE11 3TU, UK

<sup>d</sup> Department of Civil and Environmental Engineering, BarcelonaTech, Polytechnic University of Catalonia, UPC, Jordi Girona 1-3, 08034 Barcelona, Spain

<sup>e</sup> Department of Civil Engineering, São Judas Tadeu University, 546 Taquari St., 03166-000 São Paulo, Brazil

### ARTICLE INFO

#### Keywords:

HPFRCC

Steel fibre

Chlorides

Surface corrosion

Mechanical properties

### ABSTRACT

This paper presents an investigation on steel fibre surface corrosion from a quantitative standpoint and its influence on the mechanical behaviour of uncracked high-performance fibre reinforced cementitious composites. Short straight steel fibres were used at 90, 140 and 190 kg/m<sup>3</sup> in three different mixtures. Prismatic specimens were subjected to 125 wetting–drying cycles in a 5% NaCl solution. Specimen and fibre surfaces were analysed using Scanning Electron Microscopy–Energy Dispersive Spectroscopy, while mechanical behaviour was evaluated by 3-point bending tests. Results showed the formation of corrosion spots on specimen surface, but no significant reduction on the post-cracking response.

### 1. Introduction

High-performance fibre reinforced cementitious composites (HPFRCCs) are produced by a combination of a high strength cementitious matrix and high fibre contents [1–3]. Their remarkable mechanical properties allow their application in several structural elements, such as in hot-water storage tanks, bridges reinforcement, pre-cast elements with large spans, slender box girders with less stirrups, and low-rise walls with enhanced seismic performance [4–8]. The high steel fibre content employed in the manufacturing of these elements may raise concerns regarding its resistance to corrosion and durability.

Chloride-induced corrosion is the greatest threat to the durability and integrity of steel-reinforced concrete structures [9]. Chloride transport properties in uncracked steel fibre reinforced concretes have been proven similar to the properties of unreinforced concrete [10]. Chloride penetration and diffusion into the matrix depend majorly on the microstructure of the cementitious composite, considering the bulk matrix and paste–aggregate and fibre–matrix interfaces. Fibre corrosion may affect the properties of the fibre–matrix interface, resulting in detrimental processes that impair the mechanical performance of reinforced composites [11].

Some authors [12–14] highlighted a limited corrosion on uncracked steel fibre reinforced concretes (SFRC) subjected to chloride ingress due to the discontinuous nature of discrete steel fibres. SFRCs and HPFRCCs subjected to accelerated chloride exposure indicated no sign of corrosion or limited superficial oxidation [15–18]. Uncracked SFRC subjected to wetting–drying cycles in chloride solutions were damaged slightly and presents stains on the specimen surface, suggesting an early stabilization of the steel fibre deterioration [15,19–25].

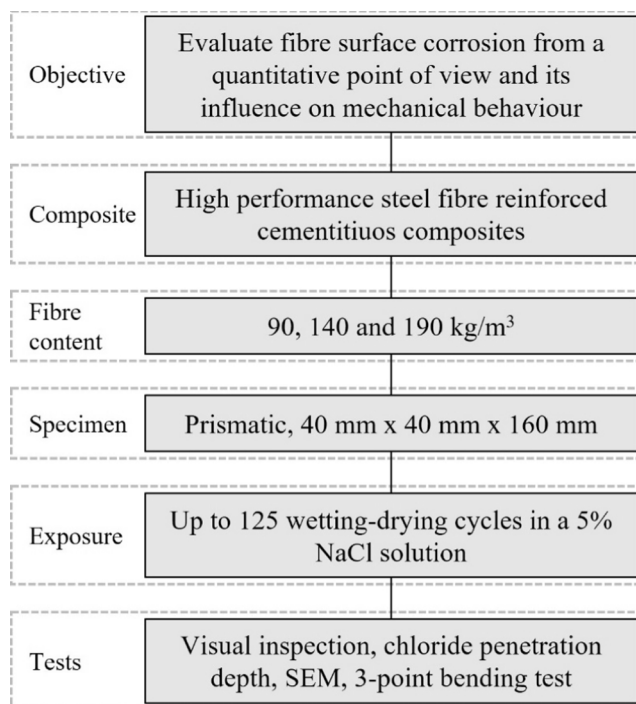
In general, the exposure of uncracked SFRC specimens to chloride solutions leads to negligible effects on the mechanical performance of the composites. SFRCs under prolonged cyclic marine exposure [26], wetting–drying cycles in chloride solutions [20,27], and immersed in salt-water [28] showed slight reductions of the residual strength due to fibre corrosion. Exposure of SFRC to wetting–drying cycles with chloride [22] and immersion in salt solution [15] presented no changes on the post-cracking behaviour. Similar outcomes have also been observed with HPFRCCs [17–18,26–27].

Table 1 summarizes recent works conducted on the evaluation of fibre corrosion in uncracked steel fibre reinforced concretes and the main tests performed in each work. Note that most studies focus on the mechanical characterization of the composite and on the evaluation of

\* Corresponding author at: Department of Civil Engineering, Campus Russas, Federal University of Ceará, UFC, Felipe Santiago 411, 62900-000 Russas, Brazil.  
E-mail address: [mylene.melo@ufc.br](mailto:mylene.melo@ufc.br) (M.M. Vieira).

**Table 1**  
Summary of recent studies on the evaluation of fibre corrosion in uncracked steel fibre reinforced concretes.

Reference	Composites analysed			Tests conducted				Quantification of specimen corrosion surface by image analysis
	SFRC	HPSFRC	UHSFRC	Surface corrosion	Chloride depth	Microscopy analysis	Mechanical behaviour	
[19,22,26,29]	•			•			•	
[30]	•			•		•		
[20]	•						•	
[31]			•	•			•	
[32]	•					•		
[14]	•						•	
[24,33]	•			•				
[17]		•		•			•	
[34]	•					•	•	
[35]			•	•	•		•	
[36]			•	•		•	•	
[27–28]	•				•		•	
This study		•		•	•	•	•	•



**Fig. 1.** Scheme of the experimental programme conducted in this study.

the specimen surface corrosion. However, only a few of them assess the chloride penetration depth and the evaluation of corrosion by microscopy analysis. In addition, no studies present a model to quantify the specimen corrosion surface by image analysis, which may be considered an important contribution of this paper.

Despite the remarkable results from the previous researches, the main mechanisms governing fibre corrosion have not been completely elucidated. Moreover, the damage level and the detrimental processes occurring in composites characterised by dense matrices and high fibre contents still need to be evaluated. Therefore, continued research on this subject is required to enhance the performance of these materials.

In this context, the objective of this paper is to investigate the fibre surface corrosion in uncracked HPFRCC specimens from a quantitative point of view and its influence on the mechanical behaviour of the composite. HPFRCCs specimens were produced with fibre contents equal to 90, 140 and 190 kg/m<sup>3</sup> and subjected to 125 wetting–drying cycles in a NaCl solution. After a determined number of wetting–drying cycles, the mechanical properties of specimens were evaluated by 3-point bending tests. After that, chloride penetration rate and depth

**Table 2**  
Properties and characteristics of steel fibres.

Property	Average results
Length (mm)	13
Diameter (mm)	0.2
Aspect ratio	62
Tensile strength (MPa)	2600
Modulus of elasticity (GPa)	200

**Table 3**  
Mix composition of HPFRCCs.

Constituent	M_90	M_140	M_190
Cement (kg/m <sup>3</sup> )	800	800	800
Silica sand (kg/m <sup>3</sup> )	1131	1108	1098
Water (kg/m <sup>3</sup> )	129	129	129
Superplasticizer (L/m <sup>3</sup> )	32	32	32
Nano-silica (L/m <sup>3</sup> )	40	40	40
Calcium carbonate (kg/m <sup>3</sup> )	200	200	200
Steel fibre (kg/m <sup>3</sup> )	90	140	190
w/c	0.23	0.23	0.23

were determined and the cross-section of the specimens was analysed by optical microscopy and scanning electron microscopy. Results obtained may lead to a more comprehensive analysis on the quantification of fibre corrosion of HPFRCCs.

## 2. Experimental methodology

This study was conducted at the Laboratory of Technology of Structures Luis Agulló at Universitat Politècnica de Catalunya (UPC) and the Scientific and Technological Center from Universitat de Barcelona (CCIT-UB). Fig. 1 presents the scheme adopted for the experimental programme conducted in this study.

### 2.1. Materials

A CEM I 52.5R Portland cement was employed to produce all the mixes. In addition, a silica sand with particle size distribution between 0.3 and 0.4 mm was used as aggregate. Ultrafine calcium carbonate (Betoflow,  $d_{50} < 5 \mu\text{m}$ ) and a suspension of nano-silica (MasterRoc® MS 685, solid content: 40%; specific weight: 1.13 g/cm<sup>3</sup>) were used to improve the packing density and mechanical properties of the mixture.

A polycarboxylate superplasticizer (Glenium ACE 425, solid content: 24.2%; specific weight: 1.04 g/cm<sup>3</sup>) was added to ensure a proper workability and to keep the water/cement ratio at 0.23 for all composites. Copper-coated short straight steel fibres (Dramix® OL13/0.20)

**Table 4**

Average results of compressive strength, dry density and water accessible porosity for M\_90, M\_140 and M\_190 at 28 days.

Test	M_90	M_140	M_190
Compressive strength (MPa)	109.7 ± 2.7	110.5 ± 1.0	112.8 ± 1.1
Dry density (g/cm <sup>3</sup> )	2.31 ± 0.03	2.33 ± 0.01	2.37 ± 0.01
Water accessible porosity (%)	13.2 ± 0.1	13.4 ± 0.3	13.6 ± 0.4

were used as a reinforcement of the specimens. The properties and characteristics of fibres are summarized in Table 2.

## 2.2. Composition and preparation of specimens

Table 3 presents the mix composition of each HPFRCC produced in this study. Fibres were used at 90 kg/m<sup>3</sup>, 140 kg/m<sup>3</sup> and 190 kg/m<sup>3</sup>, replacing sand volume with the corresponding volume of fibres. The superplasticizer dosage was kept constant at 32 L/m<sup>3</sup> for all mixtures. The nomenclature adopted to identify each mix is 'M\_fibre content'.

The preparation of HPFRCC consisted in 4 steps. Initially, cement, silica sand and calcium carbonate were added to a 1000 L vertical axis mixer and homogenized for 60 s. Then, water was added and mixed for 60 s. After that, superplasticizer and the suspension of nano silica were added and mixed for 120 s. To finish, steel fibres were added manually and mixed for 240 s. The consistency of the fresh mixtures was assessed using a flow table, according to UNE EN 12350-5 [37]. The test was adapted since no strokes were applied to the table. The spread diameters of M\_90, M\_140 and M\_190 were 215 mm, 205 mm and 240 mm, respectively, with no bleeding nor segregation.

For each mixture listed on Table 3, 5 cylindrical specimens measuring 100 mm × 200 mm (diameter × height) and 40 prismatic specimens measuring 40 mm × 40 mm × 160 mm (width × height × length) were cast according to UNE EN 12350-1 [38]. After casting, surface was finished and a curing film (MasterKure 215 WB) was sprayed over the samples to avoid water loss. Specimens were demoulded 24 h after casting. Once demoulded, specimens were stored at ambient temperature and humidity for 6 months until the date of tests.

## 2.3. Quality control of the HPFRCC

Compressive strength, dry density and water accessible porosity were used for quality control of the production process. Compressive strength was performed in an Ibertest universal testing machine model MEH-3000 according to the standard UNE EN 12390-3 [39]. 4 cylindrical specimens measuring 100 mm × 200 mm (diameter × height) were tested at 28 days at a pressure application rate equal to 0.45 MPa/s. One cylinder of each mixture was cut in four slices to determine dry density and water accessible porosity, according to UNE EN 83980 [40].

**Table 5**

Average results of flexural and residual strength after wetting–drying cycles for M\_90, M\_140 and M\_190.

Composite	Strength	Before cycles	After 5 cycles	After 35 cycles	After 65 cycles	After 95 cycles	After 125 cycles
M_90	f <sub>LOP</sub> (MPa)	15.7 ± 1.1	12.8 ± 1.4	14.1 ± 4.2	14.1 ± 5.4	15.0 ± 4.1	13.0 ± 2.3
	f <sub>R1</sub> (MPa)	15.6 ± 1.1	12.7 ± 1.1	14.0 ± 4.4	13.7 ± 5.2	12.9 ± 4.0	12.9 ± 2.4
	f <sub>R2</sub> (MPa)	13.9 ± 1.0	11.3 ± 1.1	12.5 ± 3.7	12.2 ± 4.7	12.9 ± 2.9	11.5 ± 2.3
	f <sub>R3</sub> (MPa)	11.8 ± 1.0	9.7 ± 1.6	10.9 ± 3.2	10.5 ± 3.9	10.8 ± 2.3	9.7 ± 2.0
	f <sub>R4</sub> (MPa)	10.0 ± 1.0	8.1 ± 1.7	9.3 ± 2.4	8.8 ± 3.2	8.9 ± 1.9	8.1 ± 1.7
M_140	f <sub>LOP</sub> (MPa)	17.0 ± 1.9	15.0 ± 4.7	17.0 ± 6.1	15.4 ± 2.8	16.7 ± 1.8	14.7 ± 3.3
	f <sub>R1</sub> (MPa)	16.6 ± 2.5	15.0 ± 4.6	16.5 ± 6.2	15.3 ± 2.2	16.5 ± 2.0	14.6 ± 3.6
	f <sub>R2</sub> (MPa)	13.9 ± 2.6	13.1 ± 3.9	14.6 ± 6.1	13.3 ± 1.5	13.3 ± 1.7	12.7 ± 4.6
	f <sub>R3</sub> (MPa)	10.9 ± 2.1	10.8 ± 3.1	12.0 ± 5.2	10.5 ± 1.0	10.5 ± 1.2	10.7 ± 3.7
	f <sub>R4</sub> (MPa)	8.4 ± 2.0	8.7 ± 2.5	9.6 ± 4.2	8.6 ± 0.6	8.4 ± 0.9	9.1 ± 3.4
M_190	f <sub>LOP</sub> (MPa)	18.0 ± 1.5	16.5 ± 2.9	17.9 ± 1.6	16.5 ± 2.1	18.1 ± 5.0	17.3 ± 3.1
	f <sub>R1</sub> (MPa)	18.0 ± 1.9	16.5 ± 2.6	17.5 ± 1.0	15.9 ± 2.9	18.1 ± 4.7	17.3 ± 3.4
	f <sub>R2</sub> (MPa)	15.4 ± 1.4	14.0 ± 2.3	13.5 ± 2.1	12.5 ± 1.5	15.6 ± 4.4	14.1 ± 3.2
	f <sub>R3</sub> (MPa)	12.9 ± 1.6	10.8 ± 0.9	10.6 ± 2.0	9.7 ± 0.9	12.6 ± 3.6	10.7 ± 2.5
	f <sub>R4</sub> (MPa)	10.4 ± 1.1	8.2 ± 0.6	8.4 ± 1.5	7.7 ± 1.0	10.0 ± 3.2	8.4 ± 2.3

Table 4 depicts the average values of compressive strength, dry density and water accessible porosity for each group of specimens. It may be observed that M\_90, M\_140 and M\_190 presented similar compressive strength results. This is corroborated by the uniform results obtained in the determination of dry density and water accessible porosity.

A discrete increase in water accessible porosity is observed when fibre content increases, indicating that consolidation in M\_190 was more difficult than in the other composites. In spite of that, it may be concluded that specimens were properly consolidated, independently of the fibre content employed. This is an important requirement to analyse and compare the results of chloride penetration and flexural strength.

## 2.4. Preparation of prismatic specimens for wetting–drying cycles

Prismatic specimens underwent a determined preparation before the beginning of the wetting–drying cycles. The preparation consisted in 3 steps, described in items 2.4.1 to 2.4.3.

### 2.4.1. Inductive method

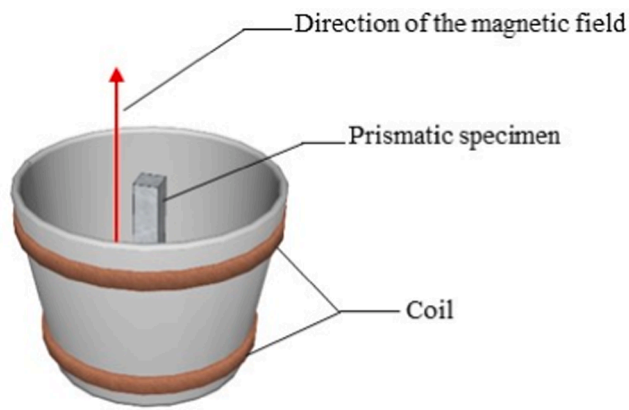
The inductive method was used to assess the amount and the orientation of steel fibres in the specimens [24,32,41]. The apparatus for the test consists of a coil acting as a sensor (Fig. 2a) and an inductance measurer. When the specimen is placed inside the coil, the magnetic field is affected by fibres and the inductance value changes. The sum of the measurements in three directions (Fig. 2b) provides information about the fibre content in the specimen. On the other hand, the relative values in each axis provide information about fibre orientation in the specimen.

The highest inductance value was observed along the x-axis of the specimen due to the preferential fibre alignment caused by the casting procedure and wall-effect of the moulds. Therefore, the inductance in the x-axis was considered for the analysis of fibre content and orientation. For each mix, a standard normal distribution regarding the inductance in the x-axis was obtained. The average inductance values for M\_90, M\_140 and M\_190, were 932 H, 1251 H and 1745 H, respectively.

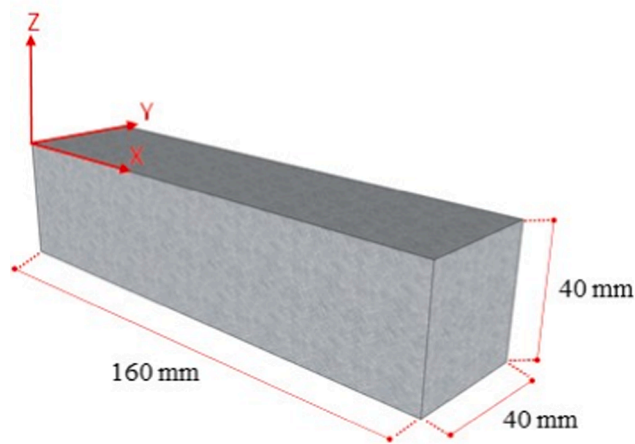
Specimens whose inductance values fell outside the limit of ±25% of the average value were considered outliers and, then, discarded. Specimens presenting inductance values within the limits were grouped in subsets according to the x-axis inductance result. This grouping aimed to guarantee that each set presented nearly the same inductance, to reduce the influence of the scatter related to fibre content and distribution on the results of the mechanical characterization.

### 2.4.2. Notching

All HPFRCC prismatic specimens were notched at midspan using a dry saw. Notches measured 2 mm in width and 6.5 mm in depth and



(a)



(b)

Fig. 2. Scheme of the inductive test method: (a) specimen inside the coil; (b) axis directions.

were required to perform the 3-point bending test. Before notching, all specimens were rotated 90° in relation to the finished surface.

#### 2.4.3. Waterproofing of the surfaces

5 faces of the prismatic specimens were waterproofed, except for the notched face. This procedure was adopted to allow chloride ingress from the notched face to the centre of the specimens. A flexible water-based epoxy membrane resistant to and several chemical attacks (including sodium chloride solution) was employed. Two coats of this membrane were applied on the specimen faces with a brush, with a 24 h interval. The membrane was cured at room temperature for 7 days, achieving a thickness of 200 µm.

#### 2.5. Wetting-drying cycles

In this experimental programme, one wetting–drying cycle lasts 96 h. Each cycle comprises the immersion of specimens in a solution for 48 h, followed by drying at room temperature for 48 h. Totally, 125 wetting–drying cycles were performed, resulting in the duration of 500 days. The whole process was conducted in a laboratory with the temperature controlled and fixed at  $(25 \pm 3) ^\circ\text{C}$ .

Wetting-drying cycles were performed in two phases. Firstly, specimens were immersed in distilled water for 48 h. Containers with the

capacity of 80 L were employed and contained 30 specimens. After this step, specimens were removed from the immersion and dried at room temperature for 48 h. This process was conducted twice to ensure a similar specimen saturation before the immersion in the NaCl solution.

The second phase comprised the immersion of specimens in a 5% NaCl solution. The concentration of the NaCl solution was selected to accelerate corrosion, considering the salt concentration in sea water equal to 3.0–3.5% by mass. Water pumps were installed inside the boxes to circulate the salt water during the wetting stage to homogenize the solution and avoid concentration variations. Adjustments of the water level and the chloride content were performed monthly, to keep NaCl concentration constant at 5% by mass. The chloride concentration was controlled by automatic titration with silver nitrate (Titrator micro TT 2050).

#### 2.6. Test methods to characterize specimens subjected to wetting–drying cycles

##### 2.6.1. Analysis of surface corrosion

Surface corrosion was analysed visually in 10 specimens of each mix, after 5, 15, 25, 35, 45, 55, 65, 75, 85 and 95 wetting–drying cycles. Pictures from the specimen face that was not waterproofed were taken and the corroded area was analysed. To identify the evolution of the corroded area, an algorithm was developed and implemented in Matlab® using the HSV (Human Visual System) colour model. The first step was to transform the image from RGB (Red, Green and Blue) to HVS and decompose it into three layers that represent the model: hue (H), saturation (S) and brightness value (V).

For each layer, the interest range is indicated by the histograms: for the hue, the pixels are separated in values from 0 (zero) to the threshold; for the saturation and brightness, pixels with values greater than the threshold are selected. After that, pixels that appear simultaneously in the range of interest of the three layers are identified as corrosion stains. The relation between the identified pixels and the total quantity of pixels of the image (resolution) defines the percentage of surface area containing corrosion stains.

##### 2.6.2. Analysis of chloride penetration depth

To evaluate the ingress of chlorides in the matrix, five 10 mm-thick slices of the cross-section area were cut from each specimen after the mechanical tests and analysed by the silver nitrate colorimetric method [43]. Each slice was sprayed with a 0.1 M silver nitrate solution, leading to the precipitation of a white solid composed by silver chloride, which was used to measure the depth of chloride penetration. This method provides a convenient a direct identification of free chloride ions in the cementitious matrix. This analysis was conducted after 5, 35, 65, 95 and 125 wetting–drying cycles.

##### 2.6.3. 3-point bending test

The influence of fibre corrosion on the post-crack behaviour of the composites was assessed by 3-point bending tests, performed based on an adaptation of the standard UNE EN 14651 [44]. 4 specimens of each mix were tested before the beginning of wetting–drying cycles and after 5, 35, 65, 95 and 125 wetting–drying cycles, using a span length equal to 100 mm. Specimens were kept at room temperature for 48 h before the test.

The load application rate was controlled by the rate of increase in the crack mouth opening displacement (CMOD), which was measured with a 5 mm-long clip-gauge. The rate of increase in CMOD was set as 0.05 mm/min up to 0.10 mm and as 0.20 mm/min beyond 0.10 mm. Load was applied perpendicularly to the finished surface and data were collected electronically at a frequency of 10 Hz. The test was finished when CMOD reached 4.0 mm.

From this test, a load-CMOD curve for each specimen was obtained. Flexural strength ( $f_{LOP}$ , limit of proportionality) was determined using equation (1), considering the first peak load. In addition, residual

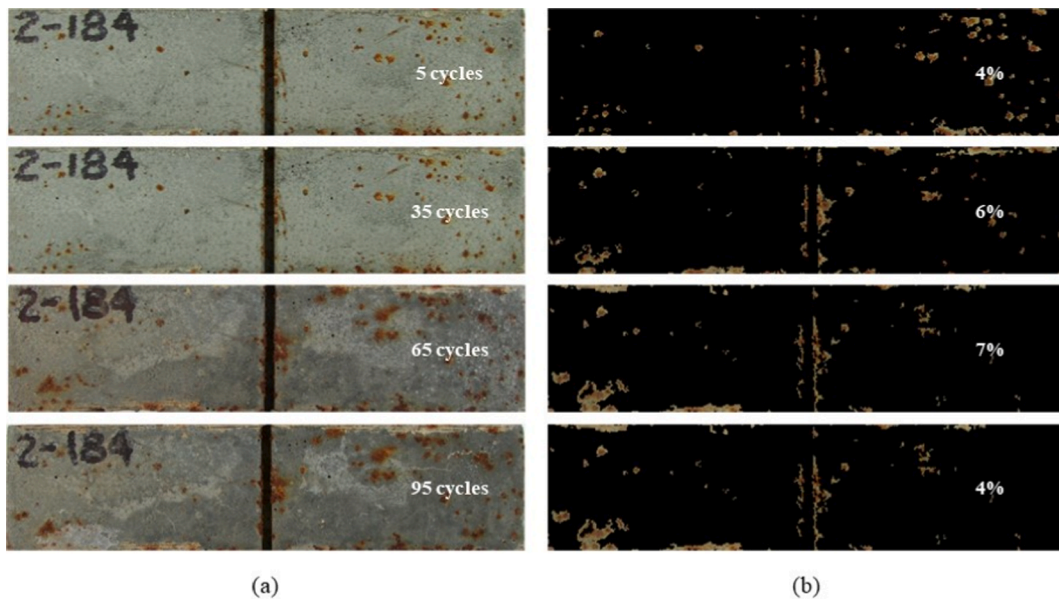


**Fig. 3.** Surface corrosion of a specimen from M\_90: (a) specimen faces in contact with the NaCl solution; (b) percentage of corroded areas detected by the algorithm developed.

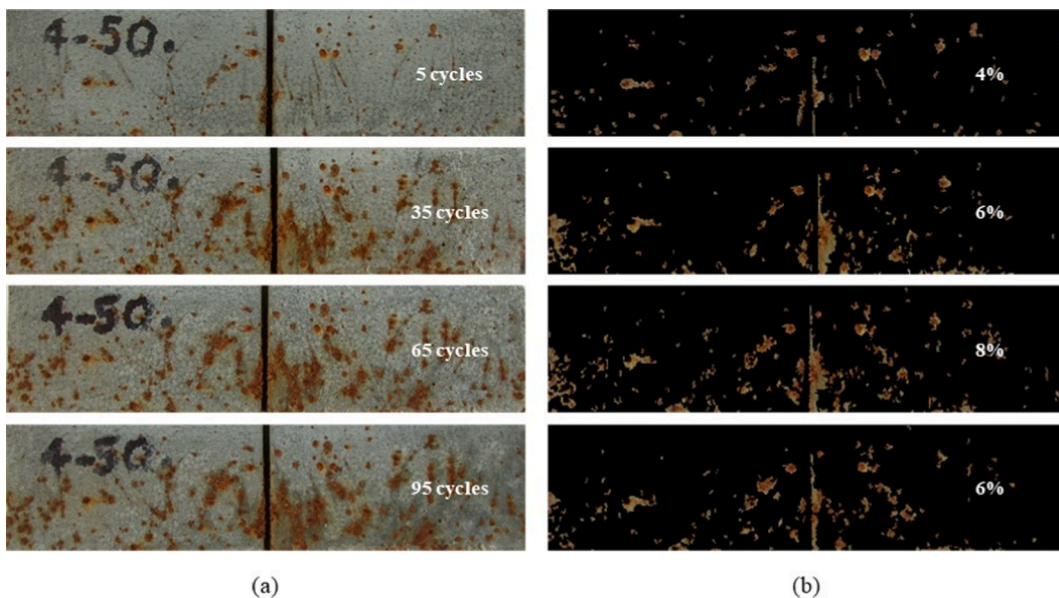


**Fig. 4.** Surface corrosion of a specimen from M\_190: (a) specimen face in contact with the NaCl solution; (b) percentage of corroded areas detected by the algorithm developed.

strengths ( $f_{R1}$ ,  $f_{R2}$ ,  $f_{R3}$  and  $f_{R4}$ ) were determined considering the load obtained when CMOD was equal to 0.5, 1.5, 2.5 and 3.5 mm, respectively. In all the cases, P represents the load (peak or residual), L is the span length (100 mm), b is the specimen width (40 mm) and  $h_{sp}$  is the distance between specimen surface and the top of the notch (33.5 mm).

$$f = \frac{3PL}{2bh_{sp}^2} \quad (1)$$

#### 2.6.4. Optical and scanning electron microscopy

After the 3-point bending test, fibre surface, specimen surface and the cross-section area at the fracture zone were analysed qualitatively by optical microscopy before the beginning of wetting–drying cycles and after 5, 95 and 125 wetting drying cycles. To complement this analysis, scanning electron microscopy (SEM) was conducted to evaluate the

evolution of fibre corrosion and the influence of chloride ingress on the microstructure of matrix. SEM was performed before the beginning of wetting–drying cycles and after 5 and 125 wetting–drying cycles. Tests were conducted in a JEOL JSM 7100F microscope at the voltage of 20 kV with samples prepared by the solvent exchange method [45] and coated with carbon. Morphology of phases was evaluated by secondary electron imaging and their chemical composition was assessed by energy dispersive X-ray analysis.

### 3. Results and discussion

#### 3.1. Analysis of surface corrosion

Fig. 3 presents the images of the exposed surface and the corroded areas detected on a specimen from mix M\_90 after 5, 35, 65 and 95

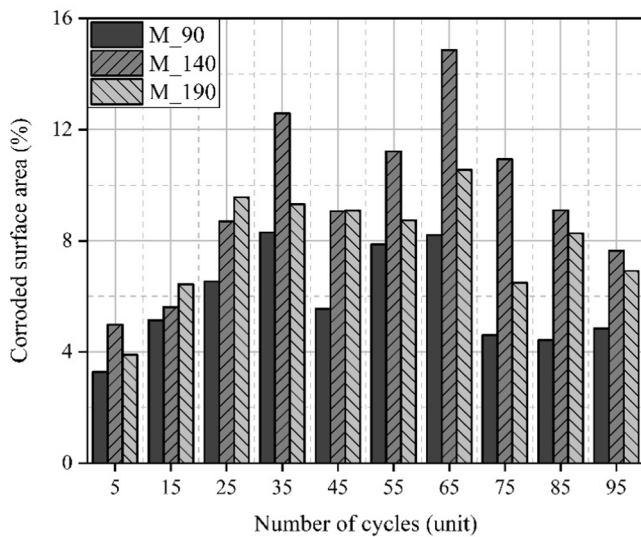


Fig. 5. Average corroded area for specimens from M\_90, M\_140 and M\_190.

wetting–drying cycles. Similarly, Fig. 4 depicts images of specimens from mix M\_190. The average corroded surface area for the specimens evaluated is presented in Fig. 5.

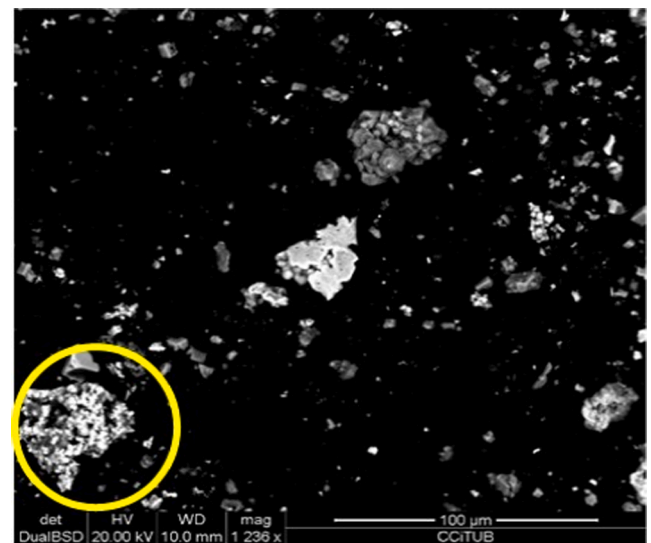
Results reveal that the number of wetting–drying cycles in the NaCl solution influences the formation of surface corrosion in specimens from M\_90, M\_140 and M\_190. Surface corrosion has been observed since cycle 5, increasing gradually until cycle 35. The ingress of water, chlorides and oxygen during wetting–drying cycles induces the corrosion of the fibres located close to the surface.

After cycle 35, a change in the increasing trend of the corroded surface area was observed. The rate of deterioration of steel fibres may have decreased due to the reduction of intact fibres close to the region in contact with the chloride solution. In addition, oxides formed by corrosion may have been leached during the wetting period due to the constant agitation induced by the pumping system.

Analysing the influence of fibre content, Fig. 5 reveals that specimens from M\_190 and M\_140 presented a more extensive surface corrosion than specimens from M\_90. Nevertheless, the increment is not directly proportional to fibre content. This fact becomes clear by observing the superior results of M\_140 in relation to M\_190. The randomness in the arrangement of fibres in the specimens is in part responsible for this phenomenon. This way, even composites with a smaller fibre volume fraction may occasionally present more fibres close to the surface in contact with the solution.

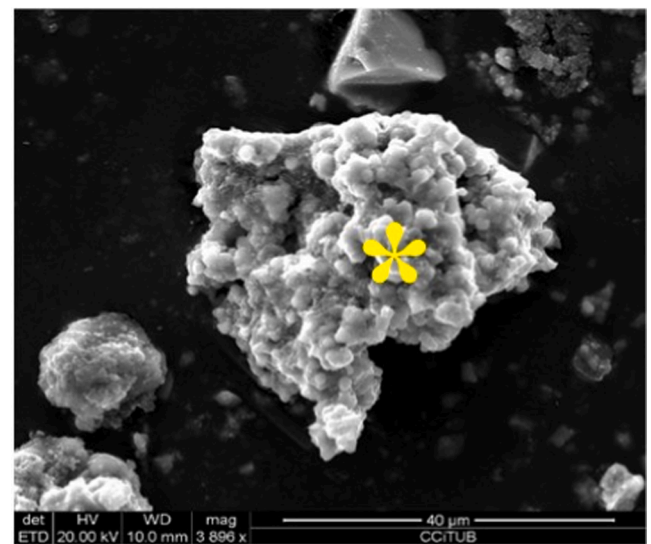
In addition, it is important to emphasize that the growth of corrosion products on the regions where fibres are overlapped is irregular and might occur at nearly the same corroded surface area. Consequently, the corroded area is not doubled, but only slightly increased. Moreover, since the deposition of corrosion products is more significant in specimens from M\_190, these oxides may be leached due to wetting–drying cycles. Therefore, the amount of oxides remaining on the surface of specimens from M\_190 may be lower than in specimens from M\_140, as observed in Fig. 5.

To detect the leaching process of corrosion products, the solids precipitated at the bottom of the containers were collected and analysed by SEM-EDS. Fig. 6 presents the SEM images and the results of the microanalysis, in terms of relative intensities obtained from the EDS spectrum, positioned above the respective image. Results revealed the presence of iron oxides, confirming that corrosion products were leached from the surfaces of the specimens during the cycles. In addition, calcium leaching from the cementitious matrix was observed. Such result suggests a reduction of the pH close to the surface of the specimen, which may further favour the corrosion process in this region.



(a)

\* Fe : Si : Cl : Ca : Na = 100 : 31.0 : 18.4 : 11.4 : 10.2



(b)

Fig. 6. SEM images of the solid phases extracted from the bottom of containers: (a) general image; (b) magnification of the circled area from image (a). EDS result corresponds to the point indicated by \* in figure (b).

### 3.2. Analysis of chloride penetration depth

Fig. 7 shows the average chloride penetration depth in the cross section of specimens from M\_190 after 5 and 125 wetting–drying cycles. The chloride penetration rate and the chloride penetration depth in specimens from M\_90, M\_140 and M\_190 are presented in Fig. 8. It must be remarked that specimens were subjected to 2 wetting–drying cycles in distilled water to ensure the same saturation condition before the beginning of the wetting–drying cycles in the NaCl solution.

Chloride penetration depth increases as fibre content increases during all cycles. As indicated in Table 4, M\_190 is 3.1 and 1.7% more porous than M\_90 and M\_140, respectively. Therefore, M\_190 presents the highest chloride penetration depth in all mixes analysed.

The highest chloride penetration rate is observed after 5 wetting–drying cycles. Such outcome may be attributed to the capillary penetration of the NaCl solution into the matrix during the first cycles.

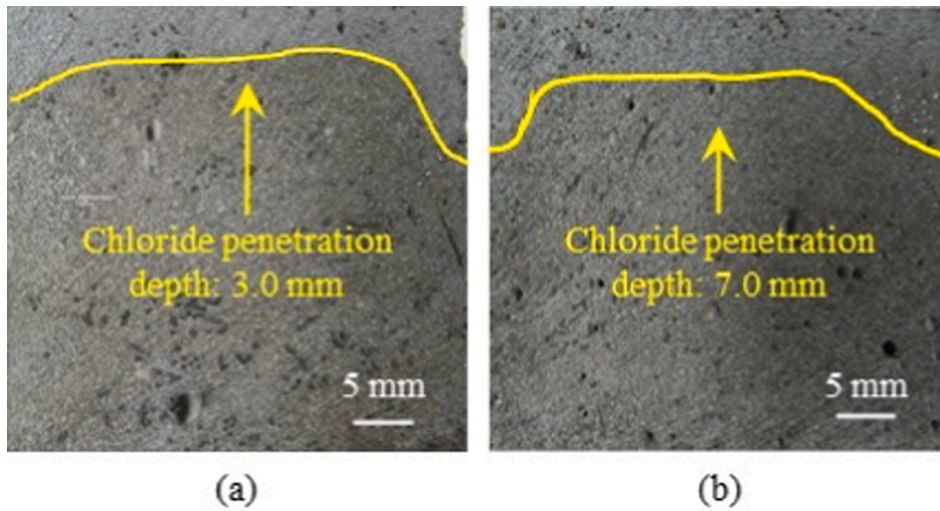


Fig. 7. Average chloride penetration depth in the cross section of specimens from M\_190: (a) after 5 wetting–drying cycles; (b) after 125 wetting–drying cycles.

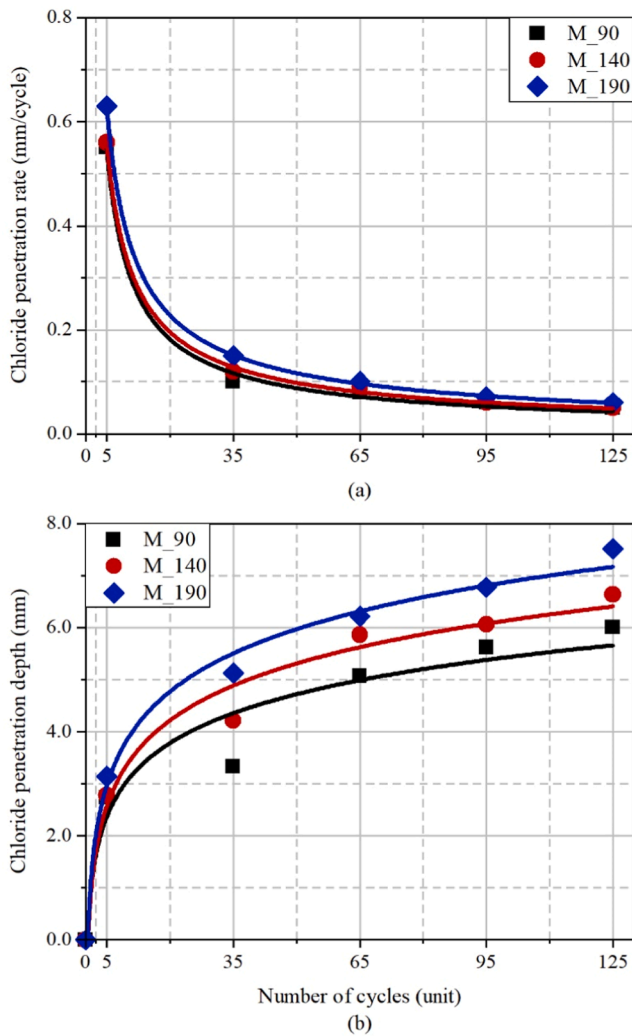


Fig. 8. Results of chloride penetration in specimens: (a) chloride penetration rate; (b) average penetration depth in the cross section of specimens.

According to Hong [46], during the wetting cycles, the dry or partially dry surface exposed to the NaCl solution absorbs the solution until saturation and the chloride concentration increases in the pores close to

the surface. During drying, water evaporates and the salts dissolved in the solution precipitate out of the deeper pores and remain inside the pores close to the surface.

Wetting–drying cycles generate a gradient of chlorides in the pores. Given the low permeability of the matrix, capillary absorption is limited to a thin layer close to the surface, in which chloride penetration is more significant during the first cycles. As wetting–drying cycles progress, an equilibrium in chloride concentration from the pore solution at the outer surface with the external media is achieved. Further chloride penetration beyond this layer is governed mostly by a diffusion process, which occurs at a lower rate when compared to capillary absorption. Therefore, a reduction in chloride penetration rate occurs, explaining the trend observed in Fig. 8.

Chloride penetration rate may also be controlled by mechanisms of chloride binding on the specimen surface. The total chloride content refers to the sum of chloride ions which are chemically bound in Friedel’s salt, chloride ions that are physically adsorbed in the diffuse layer of the C-S-H phase, and free chloride ions dissolved in the pore solution [47].

### 3.3. 3-point bending test

Fig. 9 presents the average tension-CMOD curves obtained with specimens before the beginning of wetting–drying cycles and after 5, 35, 65, 95 and 125 cycles. Each graph presents the curves obtained with M\_90, M\_140 and M\_190, grouped by the number of cycles. Table 5 presents the average results of  $f_{LOP}$ ,  $f_{R1}$ ,  $f_{R2}$ ,  $f_{R3}$  and  $f_{R4}$  for each composite and exposure condition.

The curves obtained indicate a deflection hardening behaviour for all HPRCC produced (M\_90, M\_140 and M\_190), independent of the duration of the wetting–drying cycles (5, 35, 65, 95 and 125). The average  $f_{LOP}$  before cycles increased 8% from M\_90 to M\_140 and 6% from M\_140 to M\_190. Such values, although governed by the strength of the cementitious matrix, show a tendency to increase with the incorporation of high strength fibres. As may be observed, in general, the flexural performance in terms of residual strength ( $f_{R1}$ ,  $f_{R2}$ ,  $f_{R3}$  and  $f_{R4}$ ) was higher for the largest fibre content.

Residual strength results ( $f_{R1}$ ,  $f_{R2}$ ,  $f_{R3}$  and  $f_{R4}$ ) showed that chloride penetration slightly reduced the post-cracking response of the composites M\_90 and M\_140. However, reductions did not exceed 19% in any case (i.e.: cycle or CMOD). In the case of M\_190, no significant reductions in post-cracking strength values were observed. Flexural strength results supported the observation that chloride penetration remains restricted to a thin layer close to the specimen surface. This fact

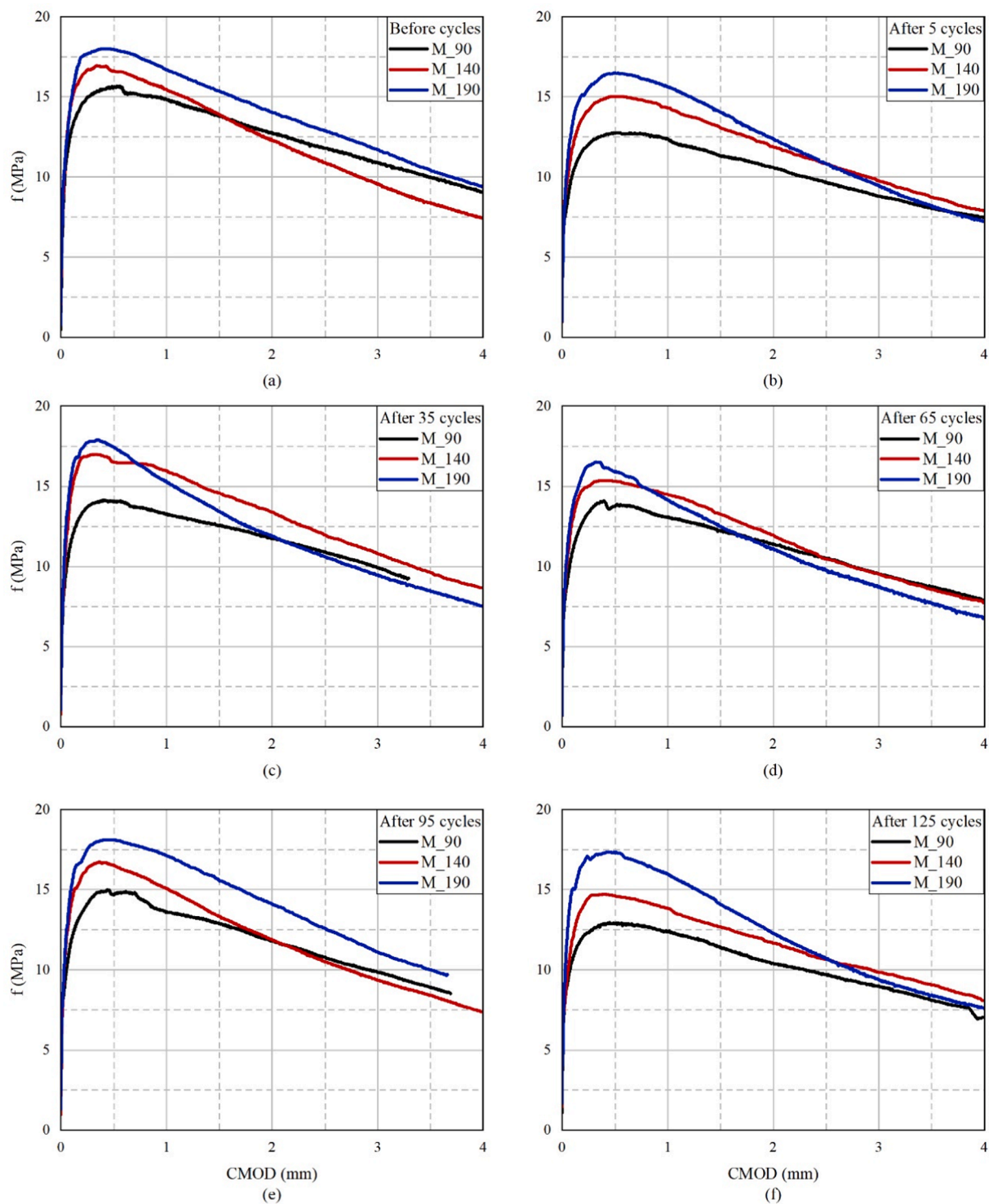


**Fig. 9.** Load-CMOD curves of specimens M\_90, M\_140 and M\_190: (a) before cycles; (b) after 5 wetting–drying cycles; (c) after 35 wetting–drying cycles; (d) after 65 wetting–drying cycles; (e) after 95 wetting–drying cycles; (f) after 125 wetting–drying cycles.

makes less evident the effect of corrosion in the composites with higher fibre contents.

### 3.4. Optical and scanning electron microscopy analyses

Fig. 10 presents images of the fibres located at the cross-section of specimens after the 3-point bending test. In addition, Fig. 11 depicts images obtained from the specimen surface in different stages. In both cases, the optical and scanning electron microscopy analyses were

conducted before the beginning of wetting–drying cycles and after 5 and 125 wetting–drying cycles. Regions analysed by EDS are indicated by an asterisk in the corresponding image. Results are represented as the relative intensities of each element, located above each image. Ca, Si, Fe, Na and Cl peaks were considered, corresponding to the energies of 3.6, 1.8, 6.3, 0.9 and 2.7 keV, respectively.

As observed in Fig. 10a, fibres from specimens before the beginning of the wetting–drying cycles do not present any signs of corrosion. This indicates they are still protected by the passivating layer formed due to

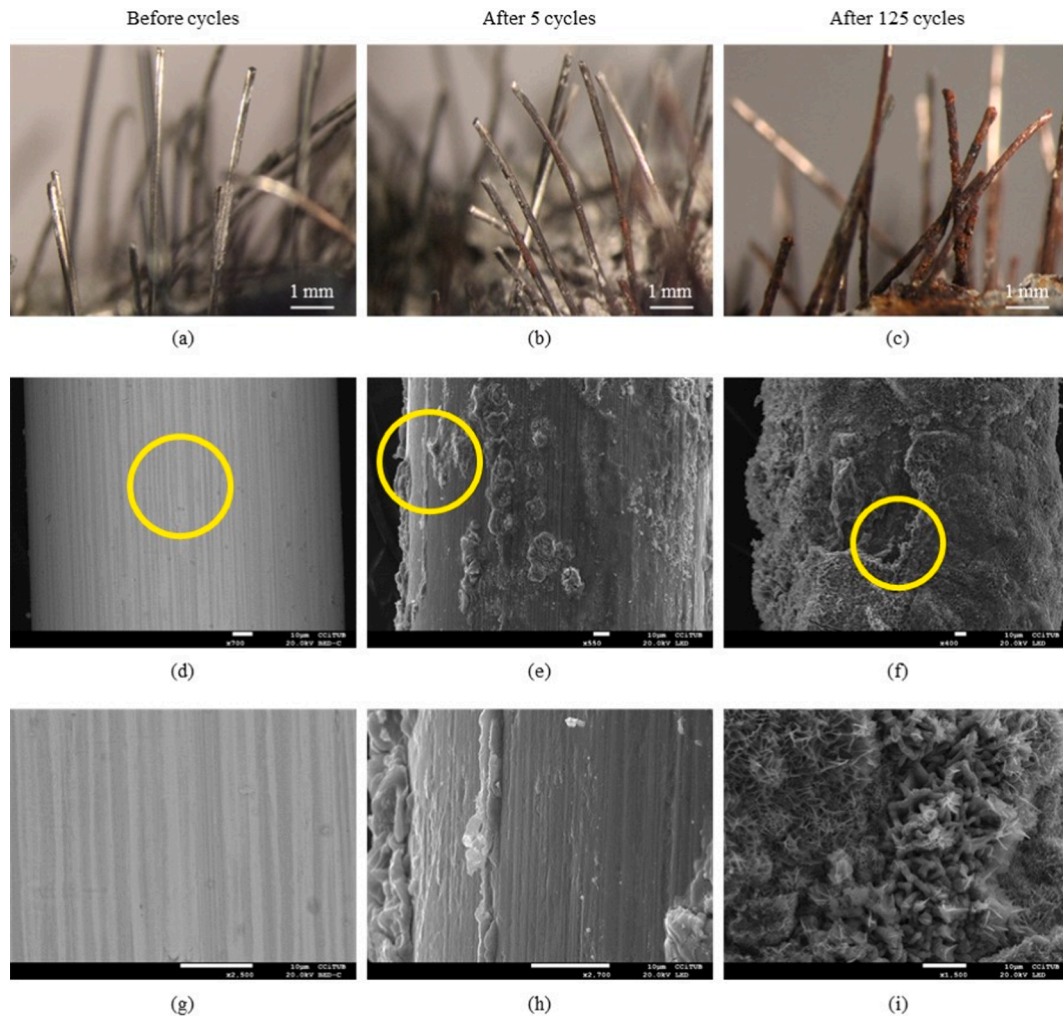


**Fig. 10.** Fibre surface from the cross-section of specimens after the 3-point bending test, before the beginning of wetting–drying cycles and after 5 and 125 wetting–drying cycles: (a, b and c) images from fibres obtained by optical microscopy; (d, e and f) images obtained by SEM; (g, h and i) magnification of the circled area from images (d, e and f), respectively.

the high alkalinity of the cementitious matrix. Fibre surface presents micro-flaws aligned with the length of the fibre as a result of the fibre manufacturing process (Fig. 10d and Fig. 10g). These micro-flaws are commonly filled with a lubricant applied in fibre production, which may lead to an incomplete or absent passivation in these regions, facilitating corrosion initiation [12].

After 5 wetting–drying cycles, a few corrosion pits are formed on the surface of some fibres close to the surface (Fig. 10b). Fibres maintain their original diameter with no significant loss of cross-section area. The corrosion level is limited due to the few wetting–drying cycles conducted until this stage and to the low permeability of the high strength matrix and the low porosity around the fibres. Fig. 10e and Fig. 10h reveal the formation of corrosion products aligned to the direction of fibre length, formed by the presence of micro-flaws on fibre surface. This may be a consequence of the unstable passivating layer in these regions, which favours steel corrosion and the consequent precipitation of corrosion products on fibre surface.

After 125 wetting–drying cycles, fibres present an extensive corrosion level (Fig. 10c). This severe corrosion level was detected in fibres positioned 0.5 mm deep from specimen surface. Although chloride penetration reached 7.0 mm in specimens (Fig. 7), the limited availability of oxygen and/or water inside the specimen may have contributed to limit corrosion.

Some regions of the fibres present localized accumulation of expansive corrosion products, increasing fibre diameter [48], indicating an accelerated corrosion process. The oxide layers present heavy cracking, tending to exfoliate and become partly or completely detached from the base steel, which in turn presents heavy pitting, corroborating results observed by de la Fuente et al [49]. The exfoliated oxide layer occurs under high concentration of chlorides and moisture.

These results may also be observed in the analysis of specimen surfaces (Fig. 11). In Fig. 11a, the fibre located at the outermost surface of the specimen is still passivated and no sign of corrosion was observed. After 5 wetting–drying cycles (Fig. 11b), a localized slight corrosion level is observed on fibre surface, detected by the SEM-EDS results obtained in Fig. 11d and Fig. 11f, presenting an elevated amount of iron. At this stage, corrosion products were not spread throughout the specimen surface.

After 125 wetting–drying cycles, a more severe fibre corrosion level was observed (Fig. 11c). As corrosion progresses, iron oxides and hydroxides spread to the regions close to fibres, filling the pores of the matrix surrounding the fibre (Fig. 11e and Fig. 11g). The corrosion layer is easily detachable from the base of the steel fibre and may be leached over cycles, limiting the amount of corrosion products on specimen surface.

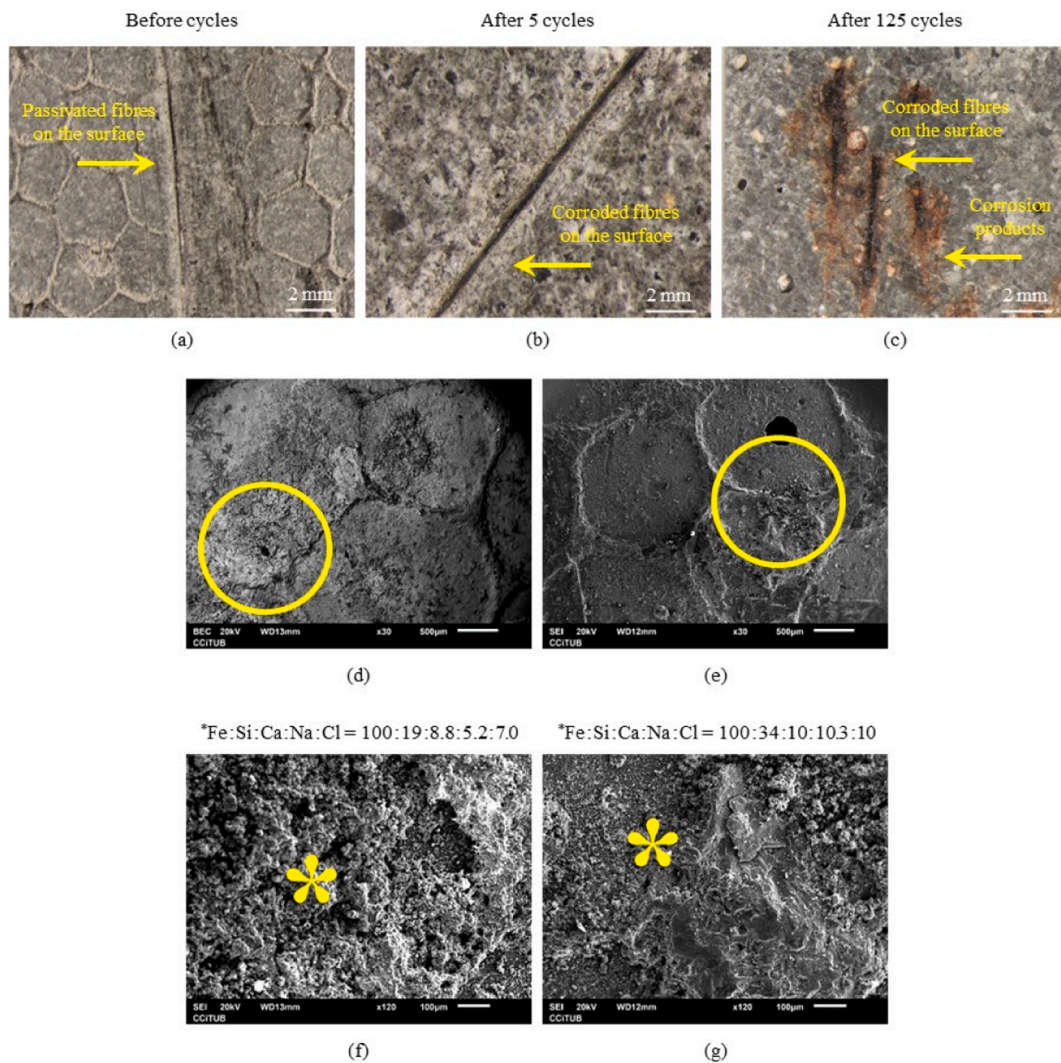


**Fig. 11.** Specimen surface before the beginning of wetting–drying cycles and after 5 and 125 wetting–drying cycles: (a, b and c) images from specimen surfaces obtained by optical microscopy; (d and e) images obtained by SEM, after 5 and 125 cycles; (f and g) magnification of the circled area from images (d and e), respectively. Asterisks represent the region analysed by EDS.

#### 4. Qualitative overview on the influence of fibre content and reaction mechanisms on fibre corrosion

Fibre corrosion mechanisms in uncracked HSPFRCC specimens were assessed considering three stages: induction, acceleration and deceleration (Fig. 12). Before the beginning of the wetting–drying cycles in the NaCl solution, fibres are protected against corrosion by the passivating layer formed on their surface due to the alkalinity of the cementitious matrix (Fig. 12a). The passivating layer is usually composed by a soluble form of  $\text{Fe}_2\text{O}_3 \cdot \text{H}_2\text{O}$  and a stable form of  $\text{Fe}_2\text{O}_3$  and [50], which reduces ion mobility between the steel and the surrounding ITZ and inhibits diffusion in the passive regions of the fibre surface.

As wetting–drying cycles progress, chlorides penetrate into the matrix by capillary absorption and diffusion, reaching fibres located close to the specimen surface (Fig. 12b). Micro-flaws present on fibre surface caused by its manufacturing process may potentially hold different ion concentrations compared to the matrix surrounding the fibre, favouring the formation of anodes and cathodes on fibre surface. When the chloride threshold concentration is exceeded, the passivating layer is compromised and corrosion starts.

The increase in the concentration of free chloride and oxygen close to fibre surface accelerates the formation of corrosion products, such as  $\text{Fe}(\text{OH})_2$ ,  $\text{Fe}(\text{OH})_3$  and  $\text{Fe}_2\text{O}_3$ , over the cycles (Fig. 12c and Fig. 12d). These

compounds have a lower specific weight than steel, resulting in expansions of around 4–6 times higher than the original volume of iron consumed in the reactions [48]. Consequently, corrosion products move to the border of the micro-flaws and spread into the pores of the ITZ and towards more superficial pores of the matrix, favoured by the moisture exchange during the wetting–drying cycles. Due to the movement of the solution during the wetting cycles, leaching occurs, removing corrosion products from fibre surface.

In the deceleration phase, fibres located close to the surface (Fig. 12e) present advanced corrosion and only small amounts of new corrosion products are generated due to the lack of iron to be oxidized. A gradual reduction trend on the amount of corrosion products on specimen surface is observed over the cycles, which may also be a consequence of the leaching process during the wetting cycles. The movement of chloride, water and oxygen towards deeper layers of the specimen is limited by the density of the matrix, thus maintaining fibres located in deep layers in a passive state or with very low levels of corrosion.

Table 6 presents a summary of the variables evaluated and their influence on surface corrosion. Ascending arrows indicate an increase in the surface corrosion in uncracked HSPFRCC specimens due to the influence of the parameter analysed, while descending arrows indicate a reduction in corrosion.

The analysis (Table 6) suggests that the surface corrosion increases

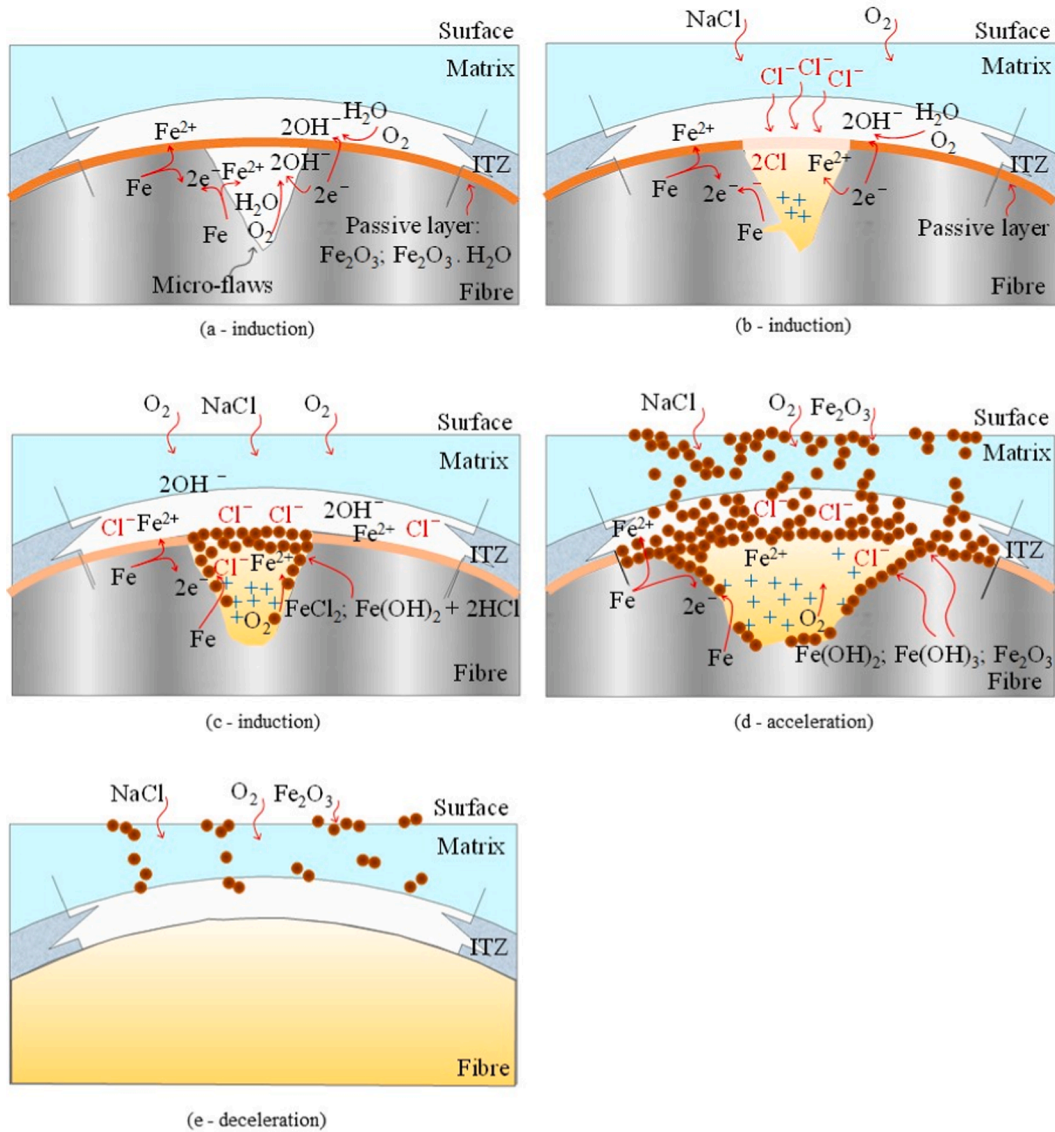


Fig. 12. Fibre surface corrosion stages in HPRFRCs: (a, b and c) corrosion induction; (d) corrosion acceleration; (e) corrosion deceleration.

Table 6

Summary of the variables evaluated and their influence on surface corrosion of specimens.

Parameter	Refer to	Effect on surface corrosion of specimens			
		Before cycles	5–35 cycles	45–65 cycles	75–95 cycles
90 kg/m <sup>3</sup> of fibre	Fig. 5	–	↑	↓	↓
140 kg/m <sup>3</sup> of fibre	Fig. 5	–	↑	↓	↓
190 kg/m <sup>3</sup> of fibre	Fig. 5	–	↑	↓	↓
Fibre corrosion induction	Fig. 12a, b, c	–	↑	–	–
Fibre corrosion acceleration	Fig. 12d	–	↑	↑	↑
Fibre corrosion deceleration	Fig. 12e	–	–	–	↓

gradually from cycle 5 until cycle 35 for the three fibre contents studied (M\_90, M\_140 and M\_190), due to corrosion induction and acceleration. These stages involve the formation of the passivating layer, chloride penetration into the cementitious matrix over cycles, the increment in the chloride threshold concentration, the breakdown of the passivating layer, the formation of corrosion products and their migration to the

superficial pores of the specimens.

From cycle 45 to cycle 65 an increase and decrease in the surface corrosion of specimens are observed for all fibre contents assessed (M\_90, M\_140 and M\_190). The stage of fibre corrosion acceleration may lead to an increment of corrosion products moving into the more superficial pores of the matrix. Besides, the leaching of corrosion products during the wetting–drying cycles decreases the amount of corrosion products observed on specimen surface.

From 75 to 95 cycles, corrosion deceleration governs fibre surface corrosion. In specimens with the smallest fibre content (M\_90), the lack of fibres close to specimen surface reduces the surface corrosion. For the highest fibre content (M\_190), corrosion products are leached from the superficial pores due to the greater number of fibres close to the surface that were corroded.

### 5. Conclusions

The following conclusions may be derived from the analysis of the experimental results:

- The approach of this research was effective in quantifying the surface corroded area of HPRFRC specimens subjected to wetting–drying in a

sodium chloride solution. Results obtained were not linearly dependent on fibre content due to the random distribution of fibres on specimen surface, the irregular growth of corrosion spots where fibres were overlapped and oxide leaching due to wetting–drying cycles.

- No reduction in the flexural behaviour of uncracked HPFRCC specimens subjected to wetting–drying cycles in a sodium chloride solution was observed. As evidenced in the analysis of the specimen fracture surface, fibre corrosion was limited to a 0.5 mm layer from specimen surface. Such observation results from the high density (low w/c ratio) and proper consolidation of the matrix, which limit chloride penetration.
- Chloride penetration showed to be more pronounced with increasing fibre contents. The highest chloride penetration rate was observed after 5 wetting–drying cycles due to the capillary penetration of the NaCl solution into the matrix. After that, chloride penetration is controlled by diffusion, reducing the chloride penetration rate.
- As presented in the qualitative overview of fibre corrosion mechanisms, corrosion comprises three main stages: induction, acceleration and deceleration. Chloride ions penetrate into a thin matrix layer close to the surface, compromising the fibre passivating layer and initiating corrosion. The increase in chloride concentration accelerates corrosion. Finally, a decrease in the corrosion takes place due to the lack of fibre to be corroded in the very superficial layer of the specimen. The dense matrix hinders deeper chloride penetration and fibre corrosion in the inner portion of the cross-section does not occur.

#### CRedit authorship contribution statement

**Mylene M. Vieira:** Conceptualization, Methodology, Formal analysis, Investigation, Writing – original draft, Writing – review & editing, Visualization. **Sergio H.P. Cavalaro:** Conceptualization, Resources, Supervision, Project administration, Funding acquisition. **Antonio Aguado:** Conceptualization, Resources, Supervision, Project administration, Funding acquisition. **Dimas A.S. Rambo:** Data curation, Writing – original draft, Writing – review & editing, Visualization. **Renan P. Salvador:** Data curation, Writing – original draft, Writing – review & editing, Visualization.

#### Declaration of Competing Interest

The authors declare that they have no known competing financial interests or personal relationships that could have appeared to influence the work reported in this paper.

#### Acknowledgements

The first author would like to thank CAPES (CAPES Foundation, Ministry of Education of Brazil, process 13117/2013-00) for the scholarship granted. Thanks, are extended to ESCOFET Company for the support in the production of the specimens.

#### References

- [1] A. Aljeboury, *Applicability of Ultra-high Performance Fibre Concrete in Structures*, Delf University of Technology, 2005.
- [2] M. van den Hurk, Slender box girders and / or less stirrups by applying HSC or HSFRC, Master Thesis, 2014.
- [3] K. Kim, G.J. Parra-Montesinos, Behavior of HPFRCC low-rise walls subjected to displacement reversals, in: Proc. Fourth Int. RILEM Work. High Perform. Fiber Reinf. Cem. Compos. 4 (HPFRCC 4), 2003: pp. 505–515.
- [4] J. Sustersic, I. Leskovar, R. Ercegovic, J. Korla, Behavior of concrete with very high fiber content, in: 7th Int. RILEM Symp. Fibre Reinf. Concr. Des. Appl., Chennai, India, 2008: pp. 183–190.
- [5] R. Yu, P. Spiesz, H.J.H. Brouwers, Mix design and properties assessment of Ultra-High Performance Fibre Reinforced Concrete (UHPRC), Cem. Concr. Res. 56 (2014) 29–39, <https://doi.org/10.1016/j.cemconres.2013.11.002>.
- [6] L. Ferrara, M. Geminiani, R. Gorleza, V. Krelani, Autogeneous self healing of high performance fibre reinforced cementitious composites, High Perform. Fiber Reinf. Cem. Compos. (HPFRCC7), Stuttgart, Ger. (2015) 71–78.
- [7] K.-H. Reineck, HPC hot-water tanks for the seasonal storage of solar heat, in: 6th Int. Symp. Util. High Strength/High Perform. Concr., Leipzig, Germany, 2002: pp. 739–753.
- [8] R. Walter, H. Stang, N. Gimsing, J.F. Olesen, High performance composite bridge decks using SCSFRC, in: 4th Int. Work. High Perform. Fiber Reinf. Cem. Compos., Ann Arbor, USA, 2003: pp. 483–504.
- [9] J.P. Broomfield, Corrosion of steel in concrete - understanding, investigation and repair, Group, Taylor & Francis, 2007.
- [10] V. Marcos-meson, A. Michel, A. Solgaard, G. Fischer, C. Edvardsen, T. Lund, Corrosion resistance of steel fibre reinforced concrete – a literature review, Cem. Concr. Compos. 103 (2018) 1–20, <https://doi.org/10.1016/j.cemconres.2017.05.016>.
- [11] A. Bentur, S. Diamond, S. Mindess, The microstructure of the steel fibre-cement interface, J. Mater. Sci. 20 (10) (1985) 3610–3620, <https://doi.org/10.1007/BF01113768>.
- [12] C. Sodeikat, C. Dauberschmidt, P. Schießl, C. Gehlen, G. Kapteina, Korrosionsmonitoring von stahlbetonbauwerken für Public Private Partnership Projekte: Dauerhaftigkeit sichtbar gemacht, Beton- Stahlbetonbau 101 (12) (2006) 932–942, [https://doi.org/10.1002/\(ISSN\)1437-100610.1002.best.v101:1210.1002.best.200600517](https://doi.org/10.1002/(ISSN)1437-100610.1002.best.v101:1210.1002.best.200600517).
- [13] P.S. Mangat, B. Molloy, Size effect of reinforcement on corrosion initiation, in: 5th Int. RILEM Symp. Fibre-Reinforced Cem. Compos., Lyon, France, 2000: pp. 691–701.
- [14] E. Nordström, Durability of Sprayed Concrete Steel Fibre Corrosion in Cracks., 2005. Ph.D. (thesis in Structural Engineering) - Lulea University of Technology, 2005.
- [15] B. Kim, A.J. Boyd, J.-Y. Lee, Durability performance of fiber-reinforced concrete in severe environments, J. Compos. Mater. 45 (23) (2011) 2379–2389, <https://doi.org/10.1177/0021998311401089>.
- [16] V. Corinaldesi, G. Moriconi, Durable fiber reinforced self-compacting concrete, Cem. Concr. Res. 34 (2) (2004) 249–254, <https://doi.org/10.1016/j.cemconres.2003.07.005>.
- [17] H. Sadeghi-Pouya, E. Ganjian, P. Claisse, K. Muthuramalingam, Corrosion durability of high performance steel fibre reinforced concrete, in: Proc. Third Int. Conf. Sustain. Constr. Mater. Technol. Kyoto, Japan—August, 2013: pp. 18–21.
- [18] S. Abbas, Structural and Durability Performance of Precast Segmental Tunnel Lining., 2014. Ph.D. (thesis in Civil and Environmental Engineering) - University of Western Ontario, 2014.
- [19] P. Serna, S. Arango, Evolution of the flexural behaviour of precracked SFRC in marine environment., in: 17th Int. RILEM Symp. Fibre Reinf. Concr. Appl. Proceedings. Chennai, India, Chennai, India, 2008: pp. 595–605.
- [20] S. Anandan, S. Vallarasu Manoharan, T. Sengottian, Corrosion effects on the strength properties of steel fibre reinforced concrete containing slag and corrosion inhibitor, Int. J. Corros. 2014 (2014), <https://doi.org/10.1155/2014/595040>.
- [21] P.S. Mangat, K. Gurusamy, Corrosion resistance of steel fibres in concrete under marine exposure, Cem. Concr. Res. 18 (1) (1988) 44–54.
- [22] A. Graeff, K. Pilakoutas, C. Lynsdale, K. Neocleous, Corrosion Durability of Recycled Steel Fibre Reinforced Concrete, in: Intersections/Intersectii, 2009: pp. 77–89.
- [23] J.-L. Granju, S. Ullah Balouch, Corrosion of steel fibre reinforced concrete from the cracks, Cem. Concr. Res. 35 (3) (2005) 572–577, <https://doi.org/10.1016/j.cemconres.2004.06.032>.
- [24] S.U. Balouch, J.P. Forth, J.-L. Granju, Surface corrosion of steel fibre reinforced concrete, Cem. Concr. Res. 40 (3) (2010) 410–414, <https://doi.org/10.1016/j.cemconres.2009.10.001>.
- [25] A. Alsaifi, S.A. Bernal, M. Guadagnini, K. Pilakoutas, Durability of steel fibre reinforced rubberised concrete exposed to chlorides, Constr. Build. Mater. 188 (2018) 130–142, <https://doi.org/10.1016/j.conbuildmat.2018.08.122>.
- [26] P.S. Mangat, K. Gurusamy, Long-term properties of steel fibre reinforced marine concrete, Mater. Struct. 20 (4) (1987) 273–282, <https://doi.org/10.1007/BF02485924>.
- [27] E. Alizade, F. Jandaghi Alaei, S. Zabihi, Effect of steel fiber corrosion on mechanical properties of steel fiber reinforced concrete, Asian J. Civ. Eng. 17 (2016) 147–158. [10.14359/51684259](https://doi.org/10.14359/51684259).
- [28] J. Carrillo, J.C. Pulido, W. Aperador, Flexural mechanical properties of steel fiber reinforced concrete under corrosive environments, Rev. Ing. Constr. 32 (2017) 59–72.
- [29] V. Marcos-Meson, G. Fischer, A. Solgaard, C. Edvardsen, A. Michel, Mechanical performance of steel fibre reinforced concrete exposed to wet–dry cycles of chlorides and carbon dioxide, Materials (Basel). 14 (2021) 13–16, <https://doi.org/10.3390/ma14102642>.
- [30] R. Roque, B. Kim, G. Lopp, Durability of Fiber-Reinforced Concrete in Florida Environments BD545-41, Tallahassee, Florida, 2009.
- [31] S. Abbas, A.M. Soliman, M.L. Nehdi, Chloride ion penetration in reinforced concrete and steel fiber-reinforced concrete precast tunnel lining segments, ACI Mater. J. 111 (2014) 613–622. [10.14359/51686991](https://doi.org/10.14359/51686991).
- [32] M. Sun, D.-J. Wen, H.-W. Wang, Influence of corrosion on the interface between zinc phosphate steel fiber and cement, Mater. Corros. 63 (1) (2012) 67–72, <https://doi.org/10.1002/maco.v63.110.1002/maco.200905580>.
- [33] C.M. V. Frazão, A. Camões, J.A.O. Barros, D. Gonçalves, Durability of steel fiber reinforced self-compacting concrete, 5th Int. Conf. Concr. Futur. (2013) 93–102.
- [34] C. Frazão, B. Díaz, J. Barros, J.A. Bogas, F. Toptan, An experimental study on the corrosion susceptibility of Recycled Steel Fiber Reinforced Concrete, Cem. Concr.

- Compos. 96 (2019) 138–153, <https://doi.org/10.1016/j.cemconcomp.2018.11.011>.
- [35] S. Pyo, T. Koh, M. Tafesse, H.K. Kim, Chloride-induced corrosion of steel fiber near the surface of ultra-high performance concrete and its effect on flexural behavior with various thickness, *Constr. Build. Mater.* 224 (2019) 206–213, <https://doi.org/10.1016/j.conbuildmat.2019.07.063>.
- [36] S. Pyo, M. Tafesse, H. Kim, H.-K. Kim, Effect of chloride content on mechanical properties of ultra high performance concrete, *Cem. Concr. Compos.* 84 (2017) 175–187, <https://doi.org/10.1016/j.cemconcomp.2017.09.006>.
- [37] AENOR, UNE-EN 12350-5:2020, Testing fresh concrete - Part 5: Flow table test, (2020). 10.1039/c0cp01060j.
- [38] AENOR, UNE-EN 12350-1:2020. Testing fresh concrete - Part 1: Sampling and common apparatus, (2020).
- [39] AENOR, UNE-EN 12390-3. Testing hardened concrete. Part 3: Compressive strength of test specimens, (2020) 24.
- [40] AENOR, UNE 83980. Concrete durability. Test methods. Determination of the water absorption, density and accessible porosity for water in concrete, (2014) 6.
- [41] S.H.P. Cavalaro, R. López-Carreño, J.M. Torrents, A. Aguado, P. Juan-García, Assessment of fibre content and 3D profile in cylindrical SFRC specimens, *Mater. Struct. Constr.* 49 (1-2) (2016) 577–595, <https://doi.org/10.1617/s11527-014-0521-2>.
- [43] C.V. Pontes, G.C. Réus, E.C. Araújo, M.H.F. Medeiros, Silver nitrate colorimetric method to detect chloride penetration in carbonated concrete: how to prevent false positives, *J. Build. Eng.* 34 (2021), 101860, <https://doi.org/10.1016/j.jobe.2020.101860>.
- [44] AENOR., UNE-EN 14651:2007+A1 Test Method for metallic fibre concrete. measuring the flexural tensile strength (limit of proportionality (LOP), residual), (2008).
- [45] R.P. Salvador, D.A.S. Rambo, R.M. Bueno, K.T. Silva, A.D. de Figueiredo, On the use of blast-furnace slag in sprayed concrete applications, *Constr. Build. Mater.* 218 (2019) 543–555, <https://doi.org/10.1016/j.conbuildmat.2019.05.132>.
- [46] K. Hong, Cyclic wetting and drying and its effects on chloride ingress in concrete, PhD thesis, 1998.
- [47] Z. Shi, M.R. Geiker, B. Lothenbach, K. De Weerd, S.F. Garzón, K. Enemark-Rasmussen, J. Skibsted, Friedel's salt profiles from thermogravimetric analysis and thermodynamic modelling of Portland cement-based mortars exposed to sodium chloride solution, *Cem. Concr. Compos.* 78 (2017) 73–83, <https://doi.org/10.1016/j.cemconcomp.2017.01.002>.
- [48] D. Chen, S. Mahadevan, Chloride-induced reinforcement corrosion and concrete cracking simulation, *Cem. Concr. Compos.* 30 (3) (2008) 227–238, <https://doi.org/10.1016/j.cemconcomp.2006.10.007>.
- [49] D. de la Fuente, I. Díaz, J. Alcántara, B. Chico, J. Simancas, I. Llorente, A. García-Delgado, J.A. Jiménez, P. Adeva, M. Morcillo, Corrosion mechanisms of mild steel in chloride-rich atmospheres, *Mater. Corros.* 67 (3) (2016) 227–238, <https://doi.org/10.1002/maco.201508488>.
- [50] R. Nishimura, N. Sato, Potential–p H diagram of composition/structure of passive films on iron, *J. Jpn. Inst. Met.* 47 (12) (1983) 1086–1093, <https://doi.org/10.2320/jinstmet1952.47.12.1086>.